IEEE Access
Multidisciplinary | Rapid Review | Open Access Journal

Received May 27, 2019, accepted June 26, 2019, date of publication July 3, 2019, date of current version July 22, 2019.

Digital Object Identifier 10.1109/ACCESS.2019.2926567

A High-Precision Method for Extracting Polarization Angle Under the Condition of Subsurface Wavefield Aliasing

JIAN LI[1,2], MING MENG[2], YAN HAN[1,2], AND XIN YAN[1]

[1]National Key Laboratory of Electronic Measurement Technology, North University of China, Taiyuan 030051, China
[2]Shanxi Key Laboratory of Information Detection and Processing, North University of China, Taiyuan 030051, China

Corresponding author: Jian Li (lijian851208@126.com)

This work was supported in part by the Shanxi Provincial Youth Fund Funding under Grant 201801D221205, in part by the Shanxi Provincial University Innovation Project Funding under Grant 201802083, in part by the "13th Five-Year" Equipment Pre-research Weapons Industry Joint Fund under Grant 6141B012904, and in part by the Equipment Pre-Research Weapon Equipment Joint Fund under Grant 6141B021303.

ABSTRACT Source location based on polarization angle information is a research hot spot in the field of shallow distributed source localization. The near-field P-wave and S-wave aliasing are severe and the polarization characteristics of the wave group are poor, making it difficult to extract the polarization angle, an important source localization parameter. To address the above difficulty, this paper proposes a method that is based on high-resolution parabolic Radon transform (HRP-Radon) and incorporates adaptive covariance matrix (ACM) to extract the polarization angle information of the wavefront. First, a data set is constructed from the data acquired by the sensor array, and this data set is morphologically corrected against the first break time information. Second, the time domain data set is converted into the Radon domain by HRP-Radon, and the direct P-wave is extracted from the aliasing information by use of the focusing characteristics of the P-wave and S-wave and the phase characteristics of the far-field P-wave. Third, a model is built using the ACM algorithm to extract the direct P-wave angle information and the angle extraction is assessed using a metric-polarization method. The numerical simulation and experimental results show that the proposed method is able to extract the wavefront angle information of the blasting near-field aliasing signal and determine the source location from the polarization angle information. This method is of practical value to the field of underground space.

INDEX TERMS Underground source location, direct P-wave angle, wavefield separation, phase feature extraction.

I. INTRODUCTION

The shallow subsurface distributed source localization involves a large number of sensor nodes that are buried at different depths in the underground near-field monitoring area, and a wireless network is built up in a self-organization and multi-hop mode, which works in a collaborative way to sense, monitor, collect, process, and transmit the vibration signal generated from the source, and the information collected by each node is analyzed for its characteristics which are then used to locate the source [1]. Compared with the large area, large-equivalent, great-depth vibration monitoring technique applied to earthquakes, deep coal mining, or oil exploration, the shallow distributed source location comes with the following features: (1) The distribution range is comparatively small, making this a small area monitoring [2]; (2) The depth of underground vibration is shallow, typically not exceeding 100m, hence a sort of shallow underground vibration; (3) the vibration wave group is complex in aliasing and, as the near-field soil, due to its constitutive characteristics, is elastoplastic, the elastic wave is much affected as a result of reflection and refraction by the ground, weakening the phase. The underground source location is considered a near-field source location technology, because it attempts the localization from the field close to the source. This technology works well for source locations in directional blasting demolition of structures, underground damage, and blasting point of weapon test sites, and has become a hot spot in the field of underground location.

The associate editor coordinating the review of this manuscript and approving it for publication was Hassan Ouakad.

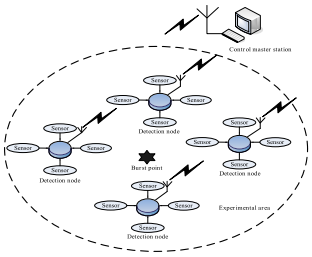

FIGURE 1. Schematic diagram of shallow underground distributed source location.

So far, the shallow distributed source location mostly draws on the deep seismic location technique by extracting differences in the time of the vibration wave reaching each node, and the source is then determined from the travel times based on Geiger theory [3]. However, in the near field there exists notable dispersion–the wave components of different frequencies propagate at different speeds, with the result that the group wave velocity is not a constant value–and this leads to a large error with the travel time location technique [4]. Unlike the far-field signal, the near-field signal has the advantages of low multi-path interference, good polarization characteristics, and a high polarization. Therefore, the angle information acquired by the sensor nodes can be used for cross-locating, which proves to be the best method for high-precision source location [5]. Moreover, this method does not require high time synchronization of the locating system, for theoretically two nodes suffice to locate the blasting. However, when applied to shallow underground location, this method faces a bottleneck. As the sensors are placed in the near field, close to the blasting source, the P-wave and the S-wave, though traveling at different speeds, tend to create aliasing, leading to inaccurate extraction of the beam angle information and hence an inaccurately ''built'' location model.

To address this problem with seismic wave angle information extraction, scholars in China and the rest of the world mostly use the multiple signal classification(MUSIC), the estimating signal parameter via rotational invariance techniques(ESPRIT), the covariance matrix reconstruction method, and the polarographic analysis method. The first three fall into the category of the far field angle estimation based on uniform linear arrays [6]. As for the polarographic analysis method the most important thing is the determination of the time window length. With strong signal aliasing, it is difficult to decide an accurate time window length in polarization analysis. Therefore, these methods are only applicable to large areas and great depths in the far field. In the near field blasting, with strong aliasing of the signal, the above methods are unable to extract satisfactory polarization angle information of the vibration wave.

In light of the above, this paper studies a method that is intended to extract the beam angle information of the near-field shock waves, a work built on the source parameter test system developed by North University of China based on the vibration sensor array.

II. THE PRINCIPLE OF BEAM DIRECTION INFORMATION EXTRACTION OF THE NEAR-FIELD SHOCK WAVE

The direct P-wave is linearly polarized when it is not coherent with other waves, that is, the medium particle vibrates in a linear trajectory about the equilibrium point. In the interior of a uniform isotropic medium, in particular, the P-wave propagates in the same direction as the particle displaces, that is, in the propagation direction of the elastic wavefront. So, the direction information of the vibration beam is found if the angle information of the direct P-wave beam is extracted satisfactorily, as shown in the following figure [7].

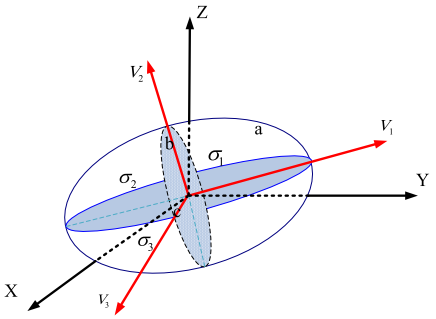

FIGURE 2. Schematic diagram of the spatial motion ellipsoid of a particle in a Cartesian coordinate system.

Due to aliasing between the P-wave and S-wave groups in the near field of blasting, to extract the direct P-wave signal from the aliased signal and to find the angle information of the direct P-wave make the two key research points of this paper.

A. EXTRACTING THE DIRECT P-WAVE FROM ALIASED SIGNALS OF A NEAR-FIELD BLASTING

The P-wave and S-wave have different focal regions in the Radon domain [8], a fact made used of in this paper to separate the two waveforms. For the aliased region in the Radon domain, the P-wave phase characteristics extracted in the far field are used to identify the focal region boundary of the near field P-wave. The process flow is shown in Fig. 3. 1. Obtain the arrival time information of the first break from the sensor array; 2. Correct the morph of the data set composed of the sensor array, adjust the offset using the arrival time information to construct an ideal parabola, and then perform HRP-Radon on the corrected data set; 3. Perform phase identification of the far field P-wave region that has been naturally separated in the data set to obtain the corresponding projection area of the region in the Radon domain, and from the projection area are obtained the focal boundary of the aliased portion of the P-wave and S-wave in the Radon domain; 4. The P-wave signal under the aliasing condition is extracted by image cutting and HRP-Radon inversion.

1) EXTRACT THE ARRIVAL TIME INFORMATION OF THE FIRST BREAK

The first break is a special type of wave. Being a vibration wave directly transmitted from the source to the receiving point, it is characterized by early take-off time and strong

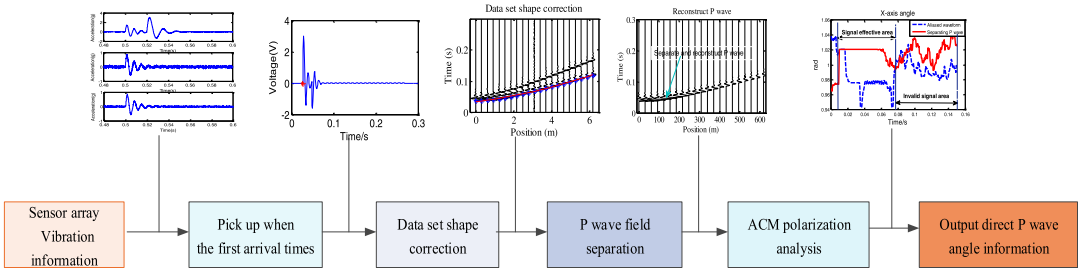

FIGURE 3. Flow chart of the extraction of the direct P-wave angle information.

energy, thus providing an important basis for determining the arrival of the vibration wave [9]. Based on the energy factor method, this paper introduces a higher order statistics and general S-transform to construct an adaptive time window, which removes the need to artificially determine the time window length while guaranteeing the time-variance of instantaneous energy factor, hence improves the pick-up accuracy of the first break.

The energy factor method is one of the most popular first break pick-up algorithms in engineering applications and its principle is shown in Fig. 4.

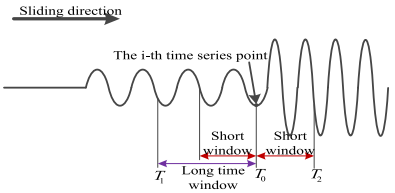

FIGURE 4. Schematic diagram of the sliding window used in the energy factor method.

Let the long/short window recognition factor $p(i)$ for the i-th time point be:

$$p(i) = \frac{\sum_{j=1}^{N} x(i+j)/N}{\sum_{j=1}^{M} x(i-j)/M} \tag{1}$$

where, $x(j)$ $(j = 1, 2, \cdots, N)$ is the vibration data, and M and N are the number of samples in the long and short time windows, respectively.

In order to obtain the first break arrival time more accurately, a higher order statistics, which is known for its enhanced mutation point, is used, and the S-transform is performed to adaptively adjust the time window length to the minimum period of the signal in the time window, thereby amplifying the time-variance of the first break detection factor. The improved first break detection factor $R(i)^{'}$ consists of three parts.

$$R(i)^{'} = P(i)^{'}.Q(i)^{'}.K(i) \tag{2}$$

where, $P(i)^{'}$ is the instantaneous energy recognition factor under unequal window lengths, $Q(i)^{'}$ is the instantaneous energy recognition factor under equal window length, $K(i)$ is kurtosis, a fourth order statistics, in the time window at the corresponding instantaneous time and they are written as:

$$P(i)^{'} = \frac{\sum_{j=-N/2}^{N/2} X^2(i+j)/N}{\sum_{j=1}^{M} X^2(i-j)/M} \tag{3}$$

$$Q(i)^{'} = \frac{\sum_{j=-N/2}^{N/2} X^2(i+j)/N}{\sum_{j=-N/2}^{N/2} X^2(i-j)/N} \tag{4}$$

$$K(i) = \frac{E[(X(i+j) - E(X(i+j)))^4]}{\{E[X(i+j) - E(X(i+j))^2]^4\}^{1/2}} \quad (j = -N/2, \cdots 0, \cdots N/2) \tag{5}$$

where, the long window length $M = 5N$ and the short window length $N = k/\Omega_i(t)$, k is the weight, and $\Omega_i(t)$ is the instantaneous dominant frequency of the i-th moment after the generalized S transform of the three-axis vibration signal [10], which refers to the frequency point with the highest energy among the wide spectrum corresponding to each moment after the generalized S transform. With the optimal matching impedance, in the near field of the blasting point, the moment the first break arrives the instantaneous dominant frequencies of the three axes are consistent [11].

$$\Omega_i(t) = \Omega_{ix}(t) = \Omega_{iy}(t) = \Omega_{iz}(t) \tag{6}$$

In the above equation, $\Omega_{ix}(t)$, $\Omega_{iy}(t)$, $\Omega_{iz}(t)$ are the instantaneous dominant frequencies of the three axes x, y and z, respectively. where, $X(i)$ is the resultant of the three energy components.

$$X(i) = (x(i) \times x(i) + y(i) \times y(i) + z(i) \times z(i))^{1/2} \tag{7}$$

In equation (7), $x(i)$, $y(i)$ and $z(i)$ are the corresponding data of the three axes. In order to accent the waveform mutation of the first break, a recognition factor $K(i)$ is constructed using the fourth order statistics kurtosis.

2) CORRECTING THE morph OF THE SENSOR ARRAY DATA SET

N sensors are laid out on a straight line on the ground surface, the coordinates $x_1, x_2, \cdots x_N$ of the N sensors being respectively noted as vector $\bar{X}$. The time $t_1, t_2, \cdots t_N$ at which the first break reaches the N sensors is respectively recorded as a vector $\bar{t}$. Where the position of each sensor node is known while that of the underground blasting point is not, the acquired data $\left(\bar{X}, \bar{t}\right)$, which can be regarded as a data set morph.

According to the theory of explosive wave propagation, when the sensor array is placed in equidistant arrangement, the relation between the first break arrival time and the propagation distance from the explosion point to the sensor nodes is approximately parabolic.

Fitting a parabola L by least squares, with L written as: $t = \tau_0 + q_0(x + a)^2$, Where τ_0 is the time intercept, q_0 is the curvature and a is a constant. Against L, correction is made to the time axis of each datum, and the corrected first break arrival time is $t_1^{'}, t_2^{'}, \cdots t_N^{'}$ respectively. The time axis of the i-th datum is translated by Δt_i, $\Delta t_i = t_i^{'} - t_i$. After the axis adjustment, $\left(\bar{X}, \bar{t}^{'}\right)$ all fall on L. Then, the time domain data is of a standard parabolic morph. In this case, the optimal Radon transform positive transform integral path is the weighted summation of the parabolic path.

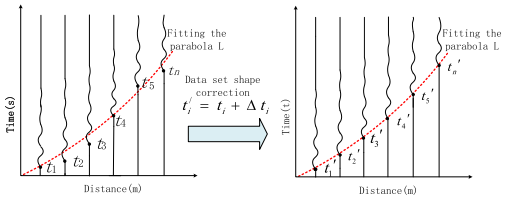

FIGURE 5. Schematic diagram of morphological correction of the data set.

After the adjustment of the time axis, $\left(\bar{X}, \bar{t}^{'}\right)$ fits the data set to L, and the sensor array data is then of a standard parabolic morph.

3) EXTRACTING THE DIRECT P-WAVE INFORMATION FROM THE ALIASED SIGNAL OF A GROUP WAVE

In this paper, the HRP-Radon transform is used in combination with far-field P-wave waveform phase characteristics to extract the near-field direct P-wave signal. Depending on the difference of the characteristic parameters (slowness, curvature, etc.) of the longitudinal and transverse waves, the HRP-Radon transform works by mapping the data set, consisting of the P-wave and the S-wave acquired by the sensor array, to the peak points of different positions in the Radon domain so that the longitudinal and transverse waves are separated [12]–[14]. The P-wave separation process is shown in Fig. 6. Firstly, the projection boundary of the P-wave in the Radon domain is found by studying the far-field P-wave vibration phase features. Secondly, the HRP-Radon transform is performed on the aliased signal data set, to get the aliased signal's focal region in the Radon domain. Thirdly, from the far-field P-wave's projection on the Radon domain, the focal region boundary of the aliased P-wave is identified, and by the image segmentation technique the focal region of the near-field P-wave is found. Finally, the P-wave signal is reconstructed with the HRP-Radon inversion.

Firstly, the three-component aliased signal is integrated from the time domain data along the parabola path to the Radon domain, to get the projection of the aliased waveforms on the Radon domain [15], [16]. The formula is as follows [17]:

$$m(q, \tau) = \int_{x\,\min}^{x\,\max} d\left(x, \tau + qx^2\right)dx \tag{8}$$

In equation (8), matrix d and m represent the data matrix of time domain and radon domain respectively. Fourier transform is performed on both sides of Eq. (8), and after that the equation is converted into a matrix form [18]:

$$M(q_j, w) = \sum_{n=1}^{N} D(x_n, w)e^{iwq_j x_n^2}, \quad j = 1, \cdots, M \tag{9}$$

$$m = L^H d \tag{10}$$

By the HRP-Radon transform, the truncation effect–due to limited spatial sampling–on the signal resolution in the Radon domain can be reduced greatly. The function in Eq. (10) can be optimized to [19], [20]:

$$m = \left(L^H L + Q_m\right)^{-1} L^H d \tag{11}$$

Operator L^H means changing data from time domain to Radon domain, and operator L means transforming data from Radon domain back to time domain. The weighted matrix Q_m is related to m as below:

$$Q_{ii} = \frac{1}{\sigma_m^2\left(1 + \frac{|m_i|^2}{\sigma_m^2}\right)} \tag{12}$$

The conjugate gradient algorithm takes up less memory but offers high computational efficiency, so in Eq. (11), the inversion of matrix $\left(L^H L + Q_m\left(m_k\right)\right)$ is done using this algorithm. The HRP-Radon transform produces a smaller data reconstruction error and entails lower energy loss in the course of transform, enabling more complete restoration of the data after transform [21] and satisfactory separation and inversion reconstruction of the P-wave.

Then, the first phase curve, the main phase curve, and the tail phase curve of the P wave are extracted. By the HRP-Radon transform, the Radon domain projections corresponding to these phase curves are obtained and used as the boundary condition for extracting the P-wave in the projection region in the Radon domain. Then, with reference to the signal characteristic boundary conditions the aliased P-wave's effective region in the Radon domain is preserved, and the P-wave inversion reconstruction is implemented having regard to this effective projection region.

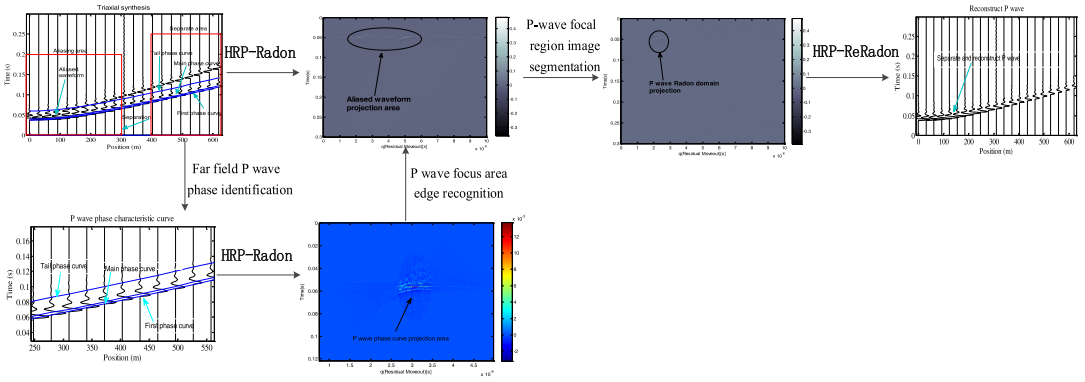

FIGURE 6. Flow chart of the direct P-wave field separation.

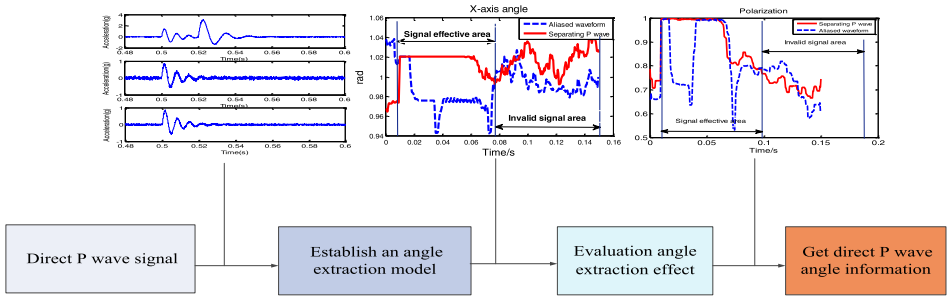

FIGURE 7. Flow chart of the extraction of the direct P-wave angle information.

Finally, the inversed and reconstructed P-wave signal is obtained by the HRP-Radon inversion (from the Radon domain to the time domain):

$$d(x,t) = \int_{q\min}^{q\max} m\left(q, t - qx^2\right)dq \tag{13}$$

The Fourier transform is performed on both sides of Eq.(13), and after that the equation is converted into a matrix [22] as follows:

$$D(x_n, w) = \sum_{j=1}^{M} M(q_j, w)e^{-iwq_j x_n^2}, \quad n = 1, \cdots, M \tag{14}$$

$$d = Lm \tag{15}$$

And the P-wave waveform after reconstruction by the Radon inversion is found by the conjugate gradient algorithm.

B. MODEL TO EXTRACT THE ANGLE INFORMATION OF THE DIRECT P-WAVE

Here, the ACM algorithm is used to extract the angle information of the P-wave. This algorithm, by use of a multi-component signal covariance matrix, makes the time window length adaptive to the minimum period of the signal in the time window, which improves the signal processing accuracy while obviates the cumbersome need of manually selecting the window length with the traditional methods. The specific extraction process using the ACM algorithm is shown in Fig. 7.

After the three-component signal $u_i(t), (i = x, y, z)$ of the P-wave being separated through the Radon transform, the Hilbert transform spectrum $u_i^h(t)$ is used to obtain its analytical signal, and the approximate expression of the multi-component signal $u_i(t)$ is used to construct the covariance matrix [23]:

$$\overline{M}(t) = \begin{vmatrix} \overline{I}_{xx}(t) & \overline{I}_{xy}(t) & \overline{I}_{xz}(t) \\ \overline{I}_{xy}(t) & \overline{I}_{yy}(t) & \overline{I}_{yz}(t) \\ \overline{I}_{xz}(t) & \overline{I}_{yz}(t) & \overline{I}_{zz}(t) \end{vmatrix} \tag{16}$$

$I_{km}(k, m = x, y, z)$ represents the covariance obtained from the data of the k and m axes. The mean value of the k-th component in the time window is μ_k.

$$I_{km}(t) = \frac{1}{T_{km}(t)} \int_{-T_{km}(t)/2}^{T_{km}(t)/2} (u_k(t+\tau) - \mu_k)(u_m(t+\tau) - \mu_m)d\tau \tag{17}$$

$T_{km}(t)$ is the adaptive window length of $\overline{M}(t)$ at time t, and is defined as [24]:

$$T_{km}(t) = \frac{6\pi N}{\Omega_x(t) + \Omega_y(t) + \Omega_z(t)} = \frac{2\pi N}{\Omega_{av}^{km}(t)} \tag{18}$$

Let the eigenvalues of the covariance matrix $\overline{M}(t)$ be $\lambda_i (i = 1, 2, 3)$ respectively, and $\lambda_1 \geq \lambda_2 \geq \lambda_3$. v_i is the corresponding characteristic vector of λ_i, and the maximum

characteristic value λ_1 corresponds to the principal characteristic vector $\mathbf{v}_1\left(v_{1x}, v_{1y}, v_{1z}\right)$. Therefore, the model for extracting the P-wave angle [25]:

$$\theta_0(t) = \arctan\left[\frac{v_{1y}(t)}{v_{1x}(t)}\right] \tag{19}$$

$$\delta_0(t) = \arctan\left[\frac{v_{1z}(t)}{(v_{1x}(t)^2 + v_{1y}(t)^2)^{1/2}}\right] \tag{20}$$

where, $\theta_0(t)$ stands for the instantaneous azimuth and $\delta_0(t)$ the instantaneous inclination. The polarization angle of the separated P-wave is extracted by the ACM algorithm, and then the polarization angle extraction performance is evaluated by the polarization angle.

Polarization, T, is a metric to measure the accuracy of the polarization angle of the P-wave. Generally, the polarization ranges between [0, 1], and the closer the polarization T is to 1, the better the polarization characteristic of the separated P-wave; when the polarization T is 0, the particle appears spatially as a sphere, that is, there is no polarization. The formula is as follows:

$$T = \frac{\left(1-\rho^2\right)^2 + \left(1-\rho_1^2\right)^2 + \left(\rho^2+\rho_1^2\right)^2}{2\left(1+\rho^2+\rho_1^2\right)^2} \tag{21}$$

where, ρ is the principal ellipticity polarization parameter, and ρ_1 is the minor ellipticity polarization parameter.

III. ALGORITHM SIMULATION AND ANALYSIS

To further verify the feasibility of the method, a three-direction elastic wave group was created by artificially simulated blasting vibration. Assuming that the underground medium was horizontally layered uniform medium, a Cartesian coordinate system was established, with the ground plane on the XOY plane and the blasting point at (0, 30, −200). Centering on the origin, 21 sensors were arranged along the X-axis at an interval of 30m. The P-wave propagated at 5500m/s, with a frequency of 150Hz and an attenuation factor of $e^{-i/160}$ $(i = 0, 1\cdots n)$. The S-wave propagated at 3800m/s, with a frequency of 120Hz and attenuation factor of $e^{-i/160}$ $(i = 0, 1\cdots n)$. The signal sampling rate was 1kHz. The sampling time was 0.3s. The noise source was Gaussian white noise, having an SNR of 30dB. The generated sensor array data is as shown in Fig. 8(a). After being morphologically corrected, the data set went through the HRP-Radon transform, to produce the corresponding focal region shown in Fig. 8(b).

From the P-wave signals in the far-field range (250m-550m) of the sensor array the phase characteristics were established, with the extracted first phase, the main phase and the tail phase as shown in Fig. 9(a). By HRP-Radon, the projection region of the data on the Radon domain is as shown in Fig. 9(b).

The image was segmented using the boundary information of the P-wave projection area shown in Fig. 9(b), and the P-wave was reconstructed by the HRP-Radon inversion, as shown in Fig. 10.

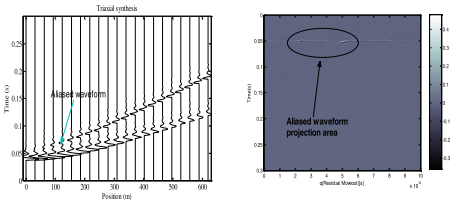

(a) Aliased waveform data (b) Aliased waveform's projection on the Radon domain

FIGURE 8. Aliased waveform time domain and its projection on the Radon domain.

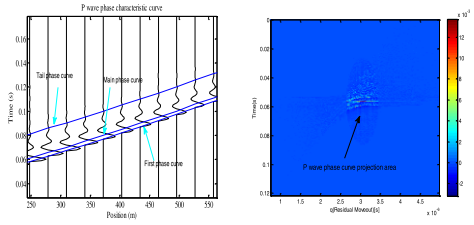

(a) P-wave phase characteristic curve (b) P-wave phase curve's projection on the Radon domain

FIGURE 9. Boundary identification of P-wave's projection on the Radon domain.

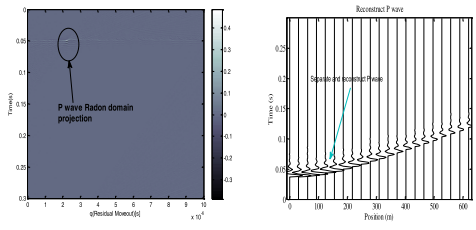

(a)Extraction of the P-wave effective region in the Radon domain (b) P-wave reconstruction through Radon inversion

FIGURE 10. Separation of the P-wave signal.

After the separation of the P-wave, the data of the fifth sensor were extracted for angle information extraction through the ACM algorithm. The coordinates of the fifth sensor were (155, 0, 0), and the angles of the blasting point to the preset x, y, and z axes of the sensor were: 1.0208 rad, 1.6976 rad, 0.5678 rad respectively. The extracted information about the instantaneous angles between the shock wave and the three axes are shown in Fig. 11.

From Fig. 11(a), in the effective period corresponding to the P-wave (0.01s-0.08s), the original aliased signal polarization curve keeps jumping between 0.75-1, showing poor polarization. After processing by the proposed method, the polarization is close to 1, suggesting that the polarization of the direct P-wave is good. The P-wave angle information is found by studying Figs. 11(b), (c), and (d), as shown in Table 1.

From Table 1 it can be seen that the proposed method can effectively extract the information of the direct P-wave angle,

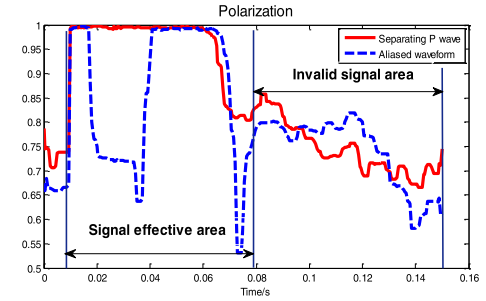

(a) Polarization curve

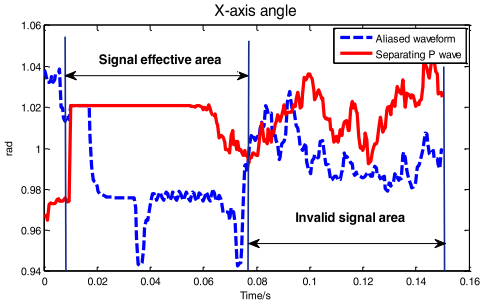

(b) X-axis instantaneous angle

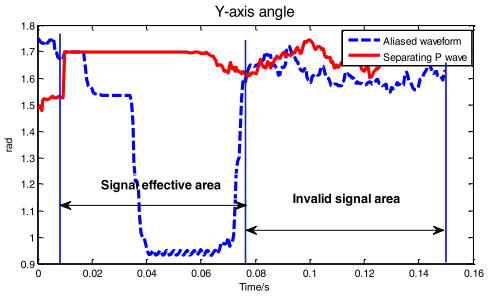

(c) Y-axis instantaneous angle

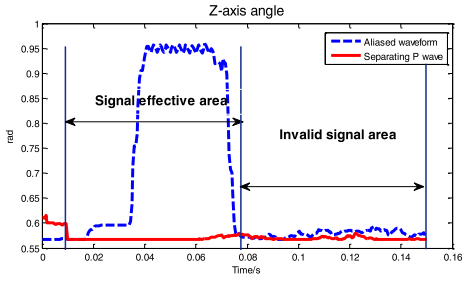

(d) Z-axis instantaneous angle

FIGURE 11. Three-axis instantaneous angles.

that is, the vibration wave beam direction, with an extraction error less than 0.001 rad for all three angles.

IV. TEST VALIDATION

To assess the feasibility of the proposed method, the source parameter acquisition system developed by the Shanxi Key Laboratory of Information Detection and Processing at North University of China was used in a validation test. The test layout is shown in Fig.12. As shown in Table 2, the sensors

TABLE 1. Polarization table of the P-wave.

	$V_x(rad)$	$V_y(rad)$	$V_z(rad)$
theoretical value	1.0208	1.6976	0.5678
measured value	1.0210	1.6980	0.5679
absolute error	0.0002	0.0004	0.0001

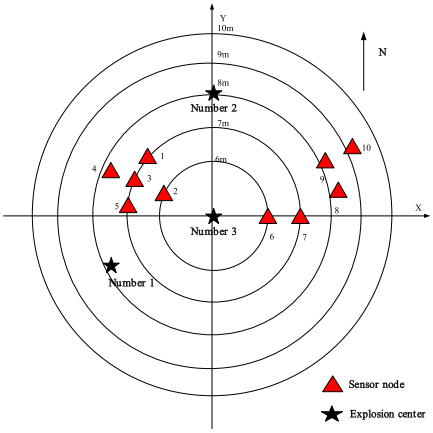

FIGURE 12. Coordinates of the sensors and the topographical map.

TABLE 2. Coordinates of the sensors.

Sensor serial number	Actual coordinates（unit：m）		
	X	Y	Z
1	-4.974	4.931	-1.121
2	-5.183	2.896	-1.687
3	-6.108	3.461	-1.304
4	-6.946	3.964	-1.292
5	-6.767	1.764	-1.096
6	6.048	0.000	-1.700
7	7.055	0.018	-1.403
8	7.753	2.151	-1.11
9	6.931	4.072	-1.09
10	7.751	4.548	-0.802

were installed at preset locations. A certain amount of TNT explosive was put underground at the preset depth as indicated in Table 3.

Guided by the preset coordinates, a universally horizontal datum was set up on the ground surface, and the sensor nodes were sequentially installed according to the sensor layout diagram. The sampling rate of the underground blasting point positioning system was set to 20 kHz, and the sampling time was 10s. The site was allowed to stand for one day, and three blasting operations were carried out one after another. The test site was as shown in Fig. 13.

The source vibration signal was obtained by the source parameter acquisition system, and the P-wave signal was extracted by HRP-Radon from the array data set, and

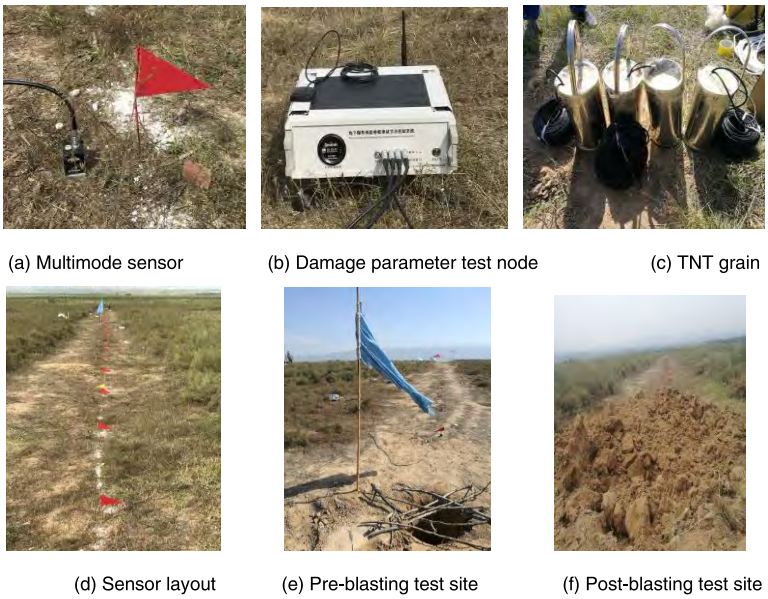

(a) Multimode sensor (b) Damage parameter test node (c) TNT grain

(d) Sensor layout (e) Pre-blasting test site (f) Post-blasting test site

FIGURE 13. Test site.

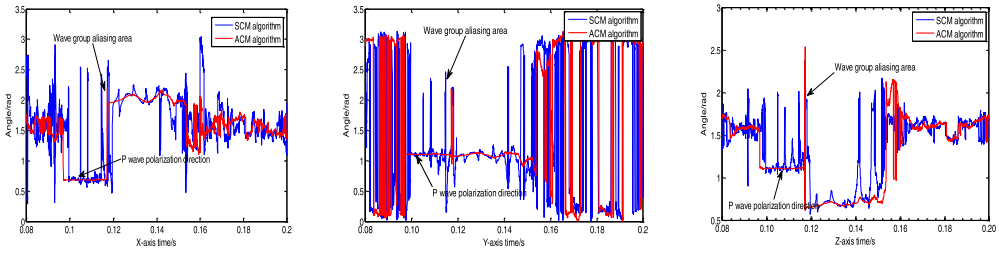

(a) X-axis instantaneous polarization map (b) Y-axis instantaneous polarization map (c) Z-axis instantaneous polarization map

FIGURE 14. Three-axis instantaneous angles.

TABLE 3. Location of the detonation point.

Serial number	Dosage (kg)	Actual coordinates（unit：m）		
		X	Y	Z
1	4	-8.636	-5.100	-2.000
2	2	-0.567	7.995	-2.000
3	2	0.000	0.000	-2.000

the P-wave angle information was extracted by the ACM. Fig. 14 shows the instantaneous angle information map corresponding to the No. 1 sensor.

The above figure shows that the instantaneous angle curves thus acquired have more stable angle information in the time zone corresponding to the direct P-wave. Table 4 shows the angle information corresponding to 10 sensor nodes sequentially extracted by this method.

As can be seen in Table 4, after the separation of the wavefield, among the sensor node group the effect of the direct P-wave angle information extraction is mixed. This is due to the coupling between the sensor and the soil varies from one node to another. The figures in bold stand for the sensors with poor polarization, which suggests poor coupling between the sensor and the soil, and the resulting amplitude characteristics are unable to characterize the movement direction of the sensor. The ones in red are two sets of sensors with the best polarization. A source location model is built up on the above sensors, as shown in Eq. 22. The equation is solved by the particle swarm optimization (PSO) algorithm, with the results as shown in Table 5.

$$\begin{cases} x_i - y_i \tan\theta_i = x - y \tan\theta_i \\ z_i = r_i \tan\varphi_i + z \\ r_i = ((x - x_i)^2 + (y - y_i)^2)^{1/2} \end{cases} \tag{22}$$

The position of the blasting point is (x, y, z), the coordinates of the node i are (x_i, y_i, z_i), and the azimuth of the p-wave beam model is θ_i (clockwise with respect to the magnetic north), and the inclination is φ_i. Table 5 shows that the proposed method copes well with the challenge of extracting the direction information of the near-field shock wave. A direction of arrival (DOA)location model has been

TABLE 4. The P-wave angle information of the node group (unit: rad).

		First hair		Second hair		Third hair	
Numbering	Polarization	Pitch angle	Azimuth	Pitch angle	Azimuth	Pitch angle	Azimuth
1	0.7920	0.0848	0.3539	0.0903	1.1107	0.0734	2.3744
2	0.1572	0.0774	0.462	0.0362	0.773	0.053	2.0774
3	0.9539	0.0622	0.328	0.0753	0.968	0.1019	2.0857
4	0.9856	0.0767	0.1782	0.0941	1.0723	0.0537	2.0829
5	0.2553	0.1225	0.2693	0.099	0.8115	0.1316	1.8607
6	0.9123	0.058	1.212	0.03	2.486	-0.0388	1.6028
7	0.9618	0.0562	1.2341	0.054	2.4153	0.0985	1.5533
8	0.9913	0.0642	1.1457	0.0923	2.2115	0.1242	1.3014
9	0.9903	0.0619	1.0204	0.1151	2.0834	0.1558	1.0639
10	0.98	0.0746	1.0062	0.1294	1.9141	0.1736	1.0304

TABLE 5. Underground blasting point location (unit: m).

Numbering	Algorithm	X	Y	Z	RMSE (m)	Operation Hours (s)
1	Actual coordinates	-8.6360	-5.1000	-2.0000		
	Calculation results	-8.4400	-4.8303	-2.1792	0.2676	15.3212
2	Actual coordinates	-0.0670	7.9950	-2.0000		
	Calculation results	-0.0222	7.7461	-1.9880	0.2531	15.3212
3	Actual coordinates	0.0000	0.0000	-2.0000		
	Calculation results	-0.1427	0.01679	-1.9210	0.1159	15.3212

built that enables the near-field source location of blasting, with all positioning errors blow 30cm.

V. CONCLUSION

To solve the difficulty with wavefront polarization angle based methods in extracting the direct P-wave angle, an important parameter in locating shallow underground vibration source, this paper proposes a solution that combines the HRP-Radon and the ACM. Firstly, the sensor array data are transferred by the HRP-Radon transform to the Radon domain, then wavefield separation is performed for the P-wave and S-wave to extract the P-wave from the aliased signal. Secondly, the P-wave beam angle information is obtained by the ACM polarization analysis. Finally, the P-wave beam angle extraction effect is evaluated by the polarization. Numerical simulation and experimental validation show that the proposed method can effectively extract the P-wave beam direction information, which parameter can be relied on to locate shallow ground sources. This study is of value to source location in directional blasting demolition, underground damage, and weapon test and other applications.

ACKNOWLEDGMENT

(Jian Li and Ming Meng contributed equally to this work.)

REFERENCES

[1] X. Yang, T. Chen, and F. Liu, "Novel wireless positioning method based on joint TOA-DOA estimation," *J. Data Acquisition Process.*, 2014.
[2] H. Tang, Y. Park, and T. Qiu, "A TOA-AOA-based NLOS error mitigation method for location estimation," *EURASIP J. Adv. Signal Process.*, vol. 1, pp. 1–14, Jul. 2008.
[3] R. Zhang, W. Xia, F. Yan, and L. Shen, "A single-site positioning method based on TOA and DOA estimation using virtual stations in NLOS environment," *China Commun.*, vol. 16, no. 2, pp. 146–159, Feb. 2019.
[4] D. Meng, X. Wang, M. Huang, C. Shen, and G. Bi, "Weighted block sparse recovery algorithm for high resolution DOA estimation with unknown mutual coupling," *Electronics*, vol. 7, no. 10, p. 217, Oct. 2018.
[5] S. Gong, H. Xiong, M. Peng, X. Ding, and H. Tang, "Joint DOD and DOA estimation for bistatic multiple-input multiple-output radar target discrimination based on improved unitary ESPRIT method," *IET Commun.*, vol. 12, no. 12, pp. 1397–1405, Jul. 2018.
[6] Y. Liu, C. Liu, Y. Zhao, and J. Zhu, "Wideband array self-calibration and DOA estimation under large position errors," *Digit. Signal Process.*, vol. 78, pp. 250–258, Jul. 2018.
[7] W. Si, Z. Peng, C. Hou, and F. Zeng, "Two-dimensional DOA estimation for three-parallel nested subarrays via sparse representation," *Sensors*, vol. 18, no. 6, pp. 1806–1861, Jun. 2018.
[8] L. Guan, S. Liu, J. Chu, R. Zhang, Y. Chen, S. Li, L. Zhai, Y. Li, and H. Xie, "A novel algorithm for estimating the relative rotation angle of solar azimuth through single-pixel rings from polar coordinate transformation for imaging polarization navigation sensors," *Optik*, vol. 178, pp. 868–878, Feb. 2019.
[9] X. Feng, X. Zhang, C. Liu, D. Wang, and Q. Yang, "Separating P-P and P-SV wave by parabolic Radon transform with multiple coherence," *Chin. J. Geophys.*, vol. 54, no. 2, pp. 304–309, Feb. 2011.
[10] W. Li and J. Wang, "On inversion and Sobolev estimate results about the weighted Radon transform," *Math. Methods Appl. Sci.*, vol. 42, no. 4, pp. 1227–1235, Mar. 2019.

[11] M. M. Abedi, M. A. Riahi, and A. Stovas, "Three-parameter Radon transform in layered transversely isotropic media," *Geophys. Prospecting*, vol. 67, no. 2, pp. 395–407, Feb. 2019.
[12] J. Liu, X. Zeng, J. Xia, and M. Mao, "The separation of P-S-wave components from three-component crosswell seismic data," *J. Appl. Geophys.*, vol. 82, pp. 163–170, Jul. 2012.
[13] J. Ivanov, R. D. Miller, D. Feigenbaum, S. L. Morton, S. L. Peterie, and J. B. Dunbar, "Revisiting levees in southern Texas using Love-wave multichannel analysis of surface waves with the high-resolution linear Radon transform," *Interpretation*, vol. 5, no. 3, pp. T287–T298, Aug. 2017.
[14] X. Jiang, F. Zheng, H. Jia, J. Lin, and H. Yang, "Time-domain hyperbolic Radon transform for separation of P-P and P-SV wavefields," *Studia Geophysica et Geodaetica*, vol. 60, no. 1, pp. 91–111, Jan. 2016.
[15] A. Gholami and M. Farshad, "Fast hyperbolic Radon transform using chirp-z transform," *Digit. Signal Process.*, vol. 87, pp. 34–42, Apr. 2019.
[16] C. Li and W. Yue, "High-resolution Radon transforms for improved dipole acoustic imaging," *Geophys. Prospecting*, vol. 65, no. 2, pp. 467–484, Mar. 2017.
[17] A. Gholami and T. Zand, "Three-parameter Radon transform based on shifted hyperbolas," *Geophysics*, vol. 83, no. 1, pp. V39–V48, Feb. 2018.
[18] J. Ivanov, R. D. Miller, D. Feigenbaum, S. L. Morton, S. L. Peterie, and J. B. Dunbar,, "Revisiting levees in southern Texas using love-wave multichannel analysis of surface waves with the high-resolution linear Radon transform," *Interpretation*, vol. 5, no. 3, pp. T287–T298, Aug. 2017.
[19] A. Gholami, "Deconvolutive Radon transform," *Geophysics*, vol. 82, no. 2, pp. V117–V125, Mar. 2017.
[20] A. Latif and W. A. Mousa, "An efficient undersampled high-resolution radon transform for exploration seismic data processing," *IEEE Trans. Geosci. Remote Sens.*, vol. 55, no. 2, pp. 1010–1024, Feb. 2016.
[21] M. Aharchaou and A. Levander, "A compressive sensing approach to the high-resolution linear Radon transform: Application on teleseismic wavefields," *Geophys. J. Int.*, vol. 207, no. 2, pp. 811–822, Nov. 2016.
[22] J. Ma, L. Shi, Y. Li, S. Xiao, and X. Wang, "Angle estimation of extended targets in main-lobe interference with polarization filtering," *IEEE Trans. Aerosp. Electron. Syst.*, vol. 53, no. 1, pp. 169–189, Feb. 2017.
[23] X. Jiang, J. Lin, F. Ye, and F. Zheng, "Separation of P–P and P–SV wavefields by high resolution parabolic Radon transform," *J. Appl. Geophys.*, vol. 119, pp. 192–201, Aug. 2015.
[24] J. Li, D. Wu, Y. Han, and L. Xu, "A method for extracting angle information of direct P wave in shallow burst point localization based on wireless, 'Sensor Array,'" *Sensor Rev.*, vol. 37, no. 1, pp. 61–70, 2017.
[25] T. Panigrahi, G. Panda, B. Mulgrew, and B. Majhi, "Distributed DOA estimation using clustering of sensor nodes and diffusion PSO algorithm," *Swarm Evol. Comput.*, vol. 9, pp. 47–57, Apr. 2013.

JIAN LI was born in Taiyuan, Shanxi, China, in 1985. He received the B.S. degree in information countermeasure, the M.S. degree in information and communication engineering, and the Ph.D. degree in information and communication engineering from the North University of China, Taiyuan, in 2009, 2011, and 2014, respectively. Since 2014, he has been a Lecturer with the North University of China and a Scientific Researcher with the Institute of Signal Capturing and Processing Technology, Key Laboratory of Shanxi Province, North University of China. He has authored eight articles, and holds seven patents. His research interests include innovative sensing technology and multidimensional signal processing.

MING MENG was born in Jinzhong, Shanxi, China, in 1992. She received the B.S. degree in 2014 and the bachelor's degree in electronic science and technology from the North University of China, Taiyuan, China, where she is currently pursuing the master's degree with the Department of Applied Mathematics. Her research interests include arrayed inversion reconstruction, cluster analysis, and algorithm optimization.

YAN HAN was born in Lvliang, Shanxi, China, in 1957. He received the B.S. degree in radio from the Nanjing University of Science and Technology, Nanjing, China, in 1982, the M.S. degree in weapon test from the North University of China, Taiyuan, China, in 1987, and the Ph.D. degree in signal and information processing from the Beijing Institute of Technology, Beijing, China, in 1998. From 2003 to 2015, he was a Vice President with the North University of China, where he is currently a Professor and a Doctoral Supervisor. He has authored three books, more than 60 articles, and more than five inventions. He holds many patents. His research interests include multidimensional signal processing and reconstruction, and non-destructive testing technology. He is an Editorial Board Member of many journals.

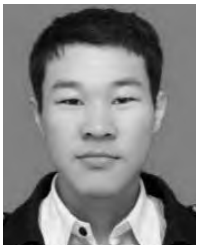

XIN YAN was born in Shanxi, China, in 1992. He received the B.S. degree in information countermeasure technology from the North University of China. He is currently pursuing the M.S. degree in electronic and communications engineering. His research interests include digital signal processing and FPGA.